iScience

CellPress
OPEN ACCESS

Article

Evolutional insights into the interaction between Rab7 and RILP in lysosome motility

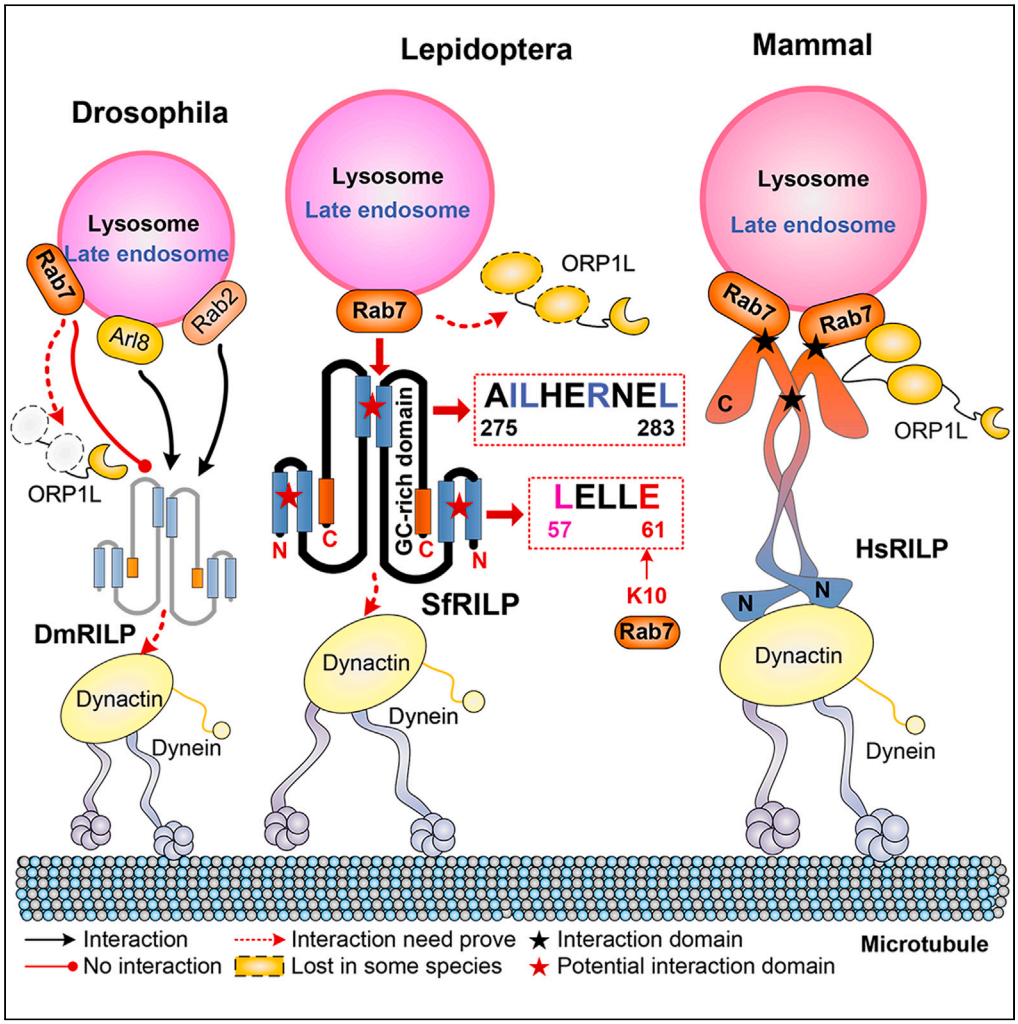

Gaofeng Cui, Zhiyan Jiang, Yaoyao Chen, ..., Ranran Sun, Xin Yi, Guohua Zhong

guohuazhong@scau.edu.cn

Highlights

Rab7-RILP interaction were features of highly evolved invertebrates and vertebrates

N-terminus of Sf-RILP was necessary for the interaction and Glu61 was the key point

GC-rich domain hampers the interaction and proved amino acids were neutral in C-terminal

RILP fragments and terminals could form homodimer in fall armyworm and fruit fly

Cui et al., iScience 26, 107040
July 21, 2023
https://doi.org/10.1016/j.isci.2023.107040

iScience

CellPress
OPEN ACCESS

Article

Evolutional insights into the interaction between Rab7 and RILP in lysosome motility

Gaofeng Cui,[1,2] Zhiyan Jiang,[1] Yaoyao Chen,[1] Yun Li,[1] Shupei Ai,[1] Ranran Sun,[1] Xin Yi,[1] and Guohua Zhong[1,3,*]

SUMMARY

Lysosome motility is critical for the cellular function. However, Rab7-related transport elements showed genetic differences between vertebrates and invertebrates, making the mechanism of lysosomal motility mysterious. We suggested that Rab7 interacted with RILP as a feature of highly evolved organisms since they could interact with each other in *Spodoptera frugiperda* but not in *Drosophila melanogaster*. The N-terminus of Sf-RILP was identified to be necessary for their interaction, and Glu61 was supposed to be the key point for the stability of the interaction. A GC-rich domain on the C-terminal parts of Sf-RILP hampered the expression of Sf-RILP and its interaction with Sf-Rab7. Although the corresponding vital amino acids in the mammalian model at the C-terminus of Sf-RILP turned to be neutral, the C-terminus would also help with the homologous interactions between RILP fragments in insects. The significantly different interactions in invertebrates shed light on the biodiversity and complexity of lysosomal motility.

INTRODUCTION

Lysosomes are highlighted as regulatory hubs for cellular and organismal homeostasis.[1,2] Endocytic, autophagic and phagocytic vesicles all move on microtubules and track to fuse with lysosomes. Lysosome-mediated signaling pathways and transcription programs are able to sense the status of cellular metabolism and control the switch between anabolism and catabolism. Lysosome positioning is a dynamically regulated process that is a crucial determinant of lysosomal function. Changes in lysosomal position within the cytoplasm are necessary for meeting other organelles, vesicles, and many factors, including cytoskeleton motor proteins, tethering factors, and SNARE proteins.[3] Dysfunction of lysosomes leads to lysosomal storage disorders in human diseases, including cancer, common neurodegenerative diseases, and metabolic diseases.[1,4]

Rab7, a fundamental element on late endosomes/lysosomes, is required for lysosome, phagolysosome and autolysosome biogenesis, and it has been shown to be important for channel trafficking and growth factor-independent survival, participating with its effectors.[5–7] In yeast, the yeast Rab7 ortholog Ypt7 is present on both membranes of vacuoles (the yeast equivalent of lysosomes) and late endosomes, where the homotypic fusion and vacuole protein sorting (HOPS) complex are supposed to connect the membranes.[8,9] This model is largely believed to hold true in metazoan systems, except for the Rab7a effector, Rab interacting lysosomal protein (RILP), together with ADP-ribosylation factor-like protein 8B (ARL8B), another small lysosomal GTPase, playing the role of HOPS receptors in mammals.[10,11] In humans, Rab7-GTP recruits RILP by specifically binding to the two typical coiled-coil regions of myosin-like protein on the C-terminus of RILP when amino acid/growth factor deficiency or protein/ROS/cholesterol accumulation occurs.[12] Then, oxysterol-binding protein (OSBP)-related protein (ORP1L) is recruited to form the RILP-Rab7-ORP1L complex, and the C-terminal of dynactin overhanging arm dynactin subunit 1 ($p150^{Glued}$) of the transporter dynein-dynactin directly interacts with the N-terminal of RILP to initiate transport. Once the complex is transferred to β-spectrin III, a receptor for dynactin on vesicles, dynein initiates late endosomal translocation to the end of microtubules.[13] In addition, another Rab7 effector, FYVE and coiled-coil domain containing 1 (FYCO1), controls plus-end directed transport via kinesins.[14] Thus, Rab7 is able to determine vesicle/lysosome bidirectional movement along microtubule tracks.[15,16] Moreover, Rab7 was suggested to recruit HOPS and connect autophagy-related gene 8 (Atg8) simultaneously through its specific effector, pleckstrin homology domain containing protein family member 1 (PLEKHM1), during the fusion of autophagosomes and lysosomes at vesicle contact sites.[17]

[1]College of Plant Protection, South China Agricultural University, Guangzhou 510642, China

[2]Guangdong Provincial Key Laboratory of Silviculture, Protection and Utilization, Guangdong Academy of Forestry, Guangzhou 510520, China

[3]Lead contact

*Correspondence: guohuazhong@scau.edu.cn

https://doi.org/10.1016/j.isci.2023.107040

Although RILP is the earliest identified and important Rab7 effector,[18,19] there is no RILP ortholog in lower eukaryotic cells, such as yeast, as well as ORP1L and the nonessential endosomal transport dynein-motor complex. CG11448, the single Drosophila ortholog of mammalian RILP, was supposed to interact with Rab2 and ARL8, another two GTPase proteins, rather than Rab7.[20] Therefore, Rab7 is still required for late endosome-lysosome fusion in Drosophila to assist in the tethering process, and the ability of RILP to bind Rab7 is supposed as a vertebrate-specific feature after the gene family expands in vertebrates.[20,21] In this study, the Rab7-related transport system was found to be different between vertebrates and invertebrates, but potentially different Rab7-RILP interaction parts and binding sites were proposed during lysosome transport in special insects. These results provide a framework for understanding the molecular basis of the Rab7-RILP interaction in invertebrates, which benefits our knowledge of the biodiversity, complexity and evolution of vacuole/lysosome motility.

RESULTS

Rab7-related transport elements showed genetic differences between vertebrates and invertebrates

Seven Rab7-related transport elements were checked among the genome data across a full breadth of animal taxonomy, including sea urchins, nematodes, insects, shrimps, birds, fishes, reptiles and mammals (Figure 1A and Table S1). There were only sole Rab7 and RILP homologs in almost all invertebrates, while those of vertebrates could be two and three or more. The motif arrangements of Rab7 were conserved among all species and homologs (Figure S1). However, the sequences of RILP varied between RILP and its orthologs (Figure 1B), as well as between insects and mammals, i.e., insect RILP homologs did not possess the RILP domain (pfam11461) or exhibited an incomplete domain (Table S2). Except for two Rab7-interacting factors of the HOPS complex, VPS39 and VPS41, the compounds showed clear differences between vertebrates and invertebrates (Figure S2 and Table S2). There was no homolog of FYCO1 in invertebrates (Figure S3), and those of ORP1L and PLEKHM1 exhibited incomplete domains or missing motifs (Figures S4 and S5). For example, insect OSBPL1A homologs had the conserved Oxysterol_BP domain (pfam01237) but lacked two regulator domains, PH_ORP1 (cd13285) and Ank_2 (pfam12796). The main PH_PLEKHM1 domain (cd13321) was absent from insect PLEKHM1 homologs. Thus, how these different elements participate in the Rab7-related bidirectional motion of vesicles/lysosomes would provide evolutionary insights into the fundamentals of related biological processes.

For further investigation, the Rab7-RILP interaction came first. Six species were selected for structure analysis: humans, mice and rats for vertebrates and fruit flies, silkworms and fall armyworms for invertebrates (Figure S6). The sequence similarity of Rab7 among the six selected species was as high as 90.14%, and it could reach 83.17% between human and fall armyworm. Except for the conserved Ras domain, the key sites of Rab7 between species were the same, such as Asn22 (N22), which helps to bind GDP and Rab7T22N is an inactive mutation; Gln67 (Q67), which plays a role in binding GTP and Rab7Q67L is an active mutation. In addition, the relative tertiary structure models of Rab7 were recorded in 1VG8, 1YHN, 1T91 and 5Z2M of the PDB database. For RILP, the amino acid sequence similarity of RILP among the selected species was 44.07%. The sequence similarity between humans and mice reached 69.58%, and that between silkworms and fall armyworms in insects was 81.04%. Although the similarity between human and fall armyworm was only 18.12%, an incomplete RILP domain was found in the C-terminal of fall armyworm. A high-similarity fragment at the N-terminus of RILP (28-70aa), especially "LELLE" at 57-61aa, appeared among these species. Furthermore, the segment "$_{IL}$XER$_{N}$EL" (251-258aa) shared similar key amino acids when comparing protein fragment 240-318aa of Hs-RILP[12] with those of Sf-RILP (Figure S7). It must be mentioned that both the nucleotides and amino acids of RILP exhibited relatively high similarity among insects, except for the appearance of a "GC-rich domain", a highly repetitive GC fragment, at the end of the C-terminal (Figure S8). The tertiary structure of RILP only showed the proven interaction parts (244-308aa in 1YHN) of mammal models in the PDB database. The structure predictions of RILP in the AlphaFold Protein Structure Database (https://alphafold.ebi.ac.uk/) were also checked. There were two coiled-coil regions in the human RILP model (Q96NA2), 28-70aa and 245-307aa, whereas there was only one domain in the RILP homolog models of fruit fly (O76878, 22-141aa) and *Caenorhabditis elegans* (G5EFB9, 17-133aa).

Sf-RILP could interact with Rab7, whereas Drosophila RILP could not

The interactions between Sf-Rab7 and the terminals and sections of Sf-RILP (Figure 2A) were screened by yeast two-hybrid systems. As shown in Figure 2B, RILP (1–1158 bp), RILP-N (1–630 bp) and RILP-C (631–1158 bp) were ligated with pGBKT7 (BD), whereas Rab7 was ligated with pGADT7 (AD). The empty AD

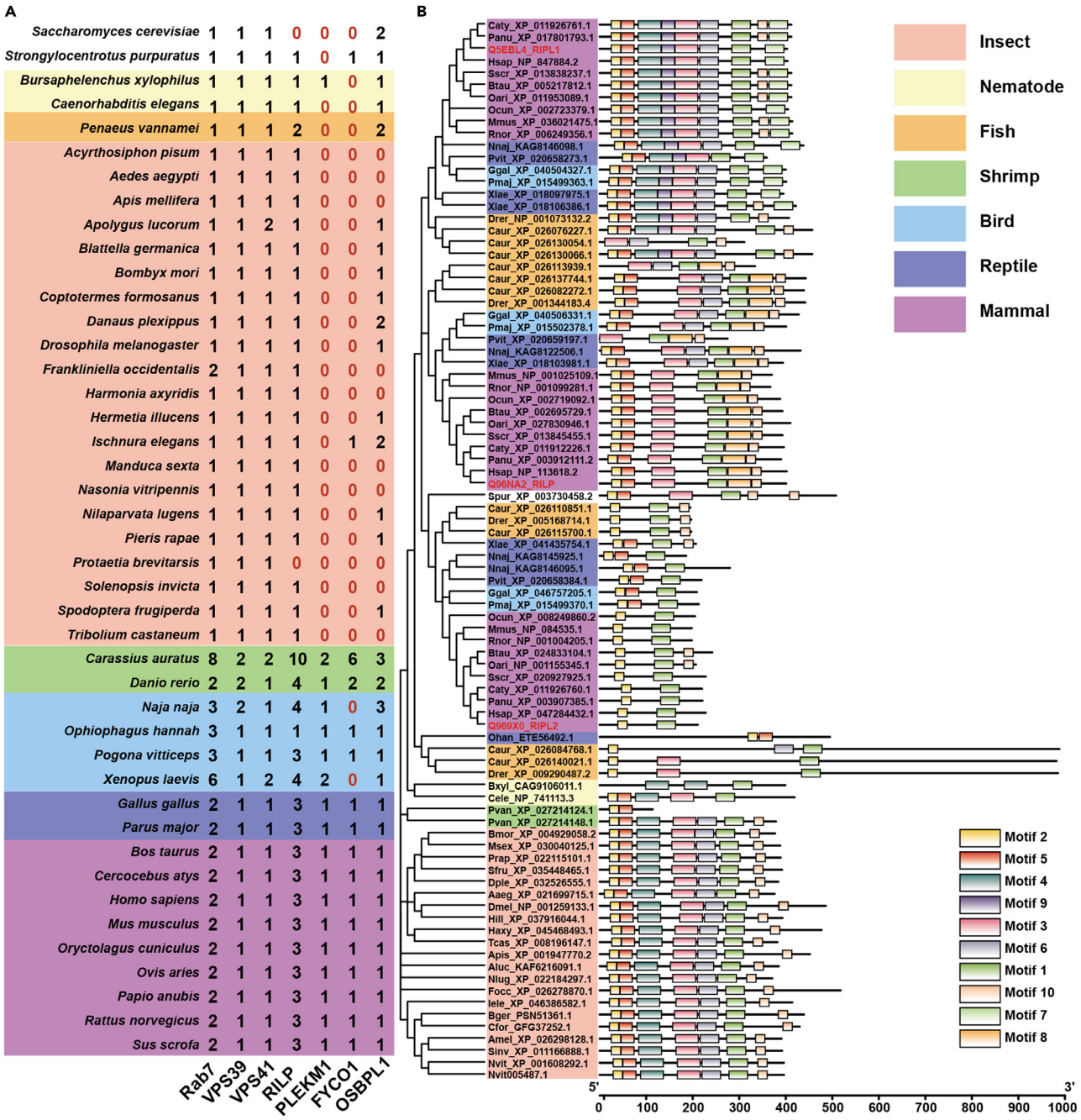

Figure 1. Rab7-related transport elements showed genetic differences between vertebrates and invertebrates

(A) Gene numbers of seven Rab7-related transport elements in the 43 selected genome datasets from vertebrates and invertebrates. No homolog was marked with "0" in red.

(B) Phylogenetic and protein motif analysis of RILP from selected species. Human homologs were marked with red.

plasmid did not interact with BD plasmids, and there were no colonies grown on the double dropout media containing X-α-Gal (DDO/X) plates. When BD plasmids were co-transformed with AD-Rab7, colonies appeared and single colonies were picked out. The interaction between RILP-N and Rab7 was identified with the presence of blue colonies on quadruple dropout media containing X-α-Gal and aureobasidin A (QDO/X/A) plates, whereas full-length RILP and RILP-C did not interact with Rab7. A similar phenomenon

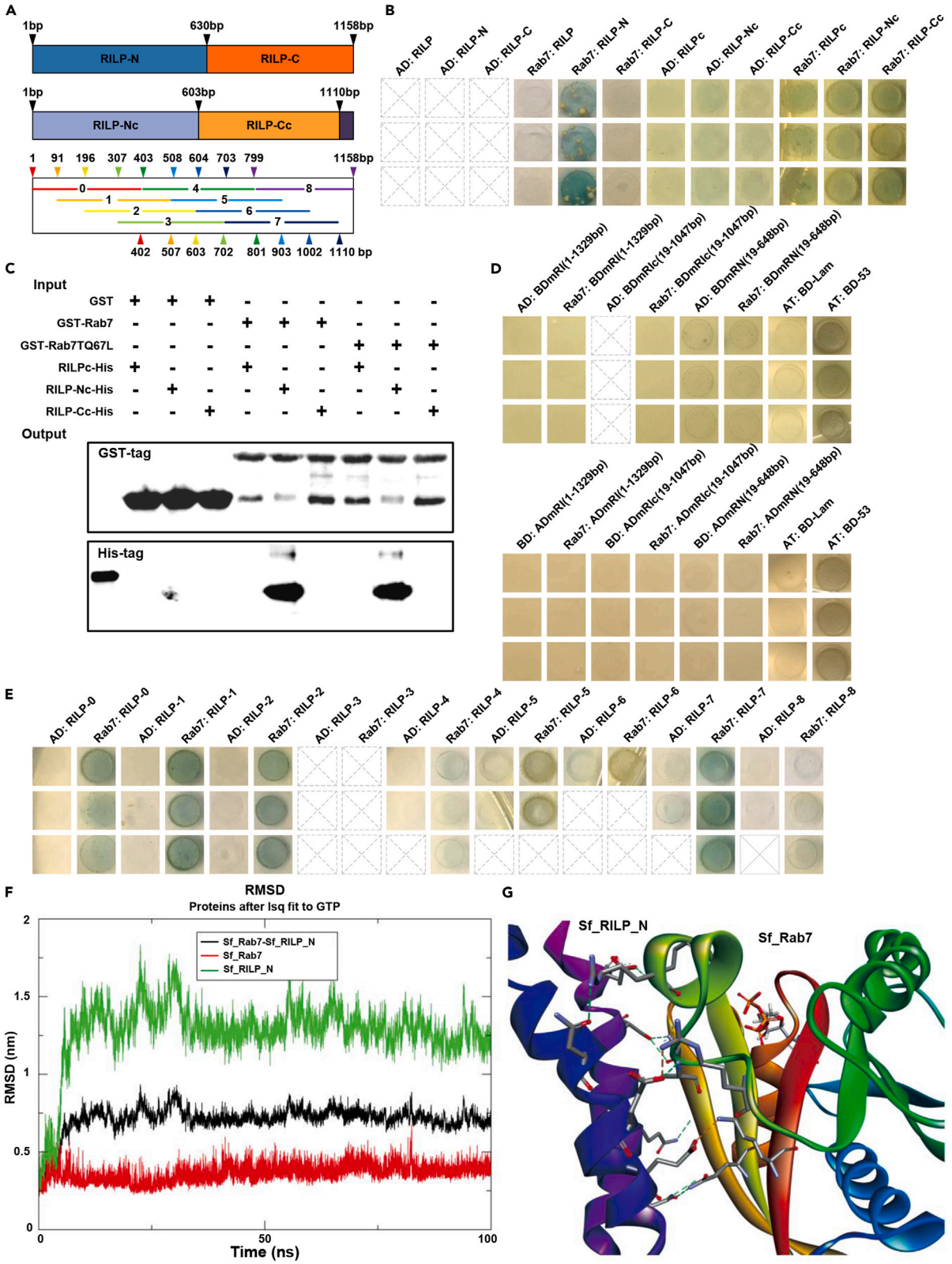
A
1bp
630bp
1158bp
RILP-N
RILP-C
1bp
603bp
1110bp
RILP-Nc
RILP-Cc
1 91 196 307 403 508 604 703 799 1158bp
0 1 2 3 4 5 6 7 8
402 507 603 702 801 903 1002 1110 bp
B
AD: RILP
AD: RILP-N
AD: RILP-C
Rab7: RILP
Rab7: RILP-N
Rab7: RILP-C
AD: RILPc
AD: RILP-Nc
AD: RILP-Cc
Rab7: RILPc
Rab7: RILP-Nc
Rab7: RILP-Cc
C
Input
GST
GST-Rab7
GST-Rab7TQ67L
RILPc-His
RILP-Nc-His
RILP-Cc-His
Output
GST-tag
His-tag
D
AD: BDmRI(1-1329bp)
Rab7: BDmRI(1-1329bp)
AD: BDmRIc(19-1047bp)
Rab7: BDmRIc(19-1047bp)
AD: BDmRN(19-648bp)
Rab7: BDmRN(19-648bp)
AT: BD-Lam
AT: BD-53
BD: ADmRI(1-1329bp)
Rab7: ADmRI(1-1329bp)
BD: ADmRIc(19-1047bp)
Rab7: ADmRIc(19-1047bp)
BD: ADmRN(19-648bp)
Rab7: ADmRN(19-648bp)
AT: BD-Lam
AT: BD-53
E
AD: RILP-0
Rab7: RILP-0
AD: RILP-1
Rab7: RILP-1
AD: RILP-2
Rab7: RILP-2
AD: RILP-3
Rab7: RILP-3
AD: RILP-4
Rab7: RILP-4
AD: RILP-5
Rab7: RILP-5
AD: RILP-6
Rab7: RILP-6
AD: RILP-7
Rab7: RILP-7
AD: RILP-8
Rab7: RILP-8
F
RMSD
Proteins after lsq fit to GTP
Sf_Rab7-Sf_RILP_N
Sf_Rab7
Sf_RILP_N
RMSD (nm)
Time (ns)
G
Sf_RILP_N
Sf_Rab7

Figure 2. The N-terminus of RILP participated in the interaction with Rab7 in insects

(A) Truncated manners and fragments characteristics of RILP for the following experiments were marked.

(B) Yeast two-hybrid systems identified the interaction of Rab7 and RILP, RILP-N, RILP-C, RILPc, RILP-Nc, and RILP-Cc on QDO/X/A plates.

(C) Protein blots of GST pull-down results for the interaction between Rab7 and RILP fragments.

(D) Yeast two-hybrid systems identified the interaction of Dm-Rab7 with whole-length Dm-RILP (1–1329 bp, DmRI), GC-rich domain-removed Dm-RILP (19–1047 bp, DmRIc) and N-terminal of Dm-RILP (19–648 bp, DmRN) on QDO/X/A plates.

(E) Yeast two-hybrid systems identified the interaction of Rab7 and truncated RILP fragments.

(F) Illustration of the RMSD on Sf-Rab7 (red), Sf-NRILP (green) and the combined system (black).

(G) Analysis of the binding mode of Sf-RILP-N recruited by Sf-Rab7. The H-bonds are marked as green dashed lines, and the salt bridges are shown as yellow dashed lines. The crossed squares mean the negative results which did not appear colonies on the DDO/X plates.

appeared in the protein expression results. Only RILP-N-His was successfully expressed at approximately 35 kDa, while RILP-His or RILP-C-His could not (Figure S9).

Then, we noticed the GC-rich domain at the C-terminus. Of interest, all three adjusted fragments, RILPc (1–1110), RILP-Nc (1–603) and RILP-Cc (604–1110), could interact with Rab7, and blue yeast colonies appeared on DDO/X and QDO/X/A plates (Figure 2B). This result suggested that the GC-rich domain at the C-terminus hampered the interaction between the two proteins, and only the truncated RILP could interact with Rab7 in fall armyworm. For protein expression, once the GC-rich domain was removed, RILPc-His and RILP-Cc-His were obtained successfully (Figures S9 and S10), suggesting that the GC-rich domain affected the protein expression of RILP. The obtained proteins were subjected to a GST pull-down assay (Figures 2C and S11). The fixed GST-tagged proteins were substantially equal to each other, and only a few His-target proteins were detected in the control groups. The Rab7-GST and Rab7Q67L-GST proteins were suggested to interact with the RILP-Nc-His, accompanied by 2 mM GTP. However, the RILPc-His and RILP-Cc-His could not be purified and their crude proteins could not interact with Rab7 in the recently GST pull-down assay.

Moreover, the corresponding Rab7 (CG5915, NM_079748.4) and RILP (CG11448, NM_130554.3) homologs of *Drosophila melanogaster* were also cloned to reveal the interaction. However, there was no interaction between Dm-Rab7 and whole-length Dm-RILP (1–1329 bp, DmRI), which was in accordance with previous reports. Moreover, neither the GC-rich domain removed Dm-RILP (19–1047 bp, DmRIc) nor the N-terminal Dm-RILP (19–648 bp, DmRN) could interact with Dm-Rab7 (Figure 2D).

The N-terminal regions of Sf-RILP facilitated the interaction with Sf-Rab7

The nucleotide sequence of Sf-RILP was cleaved into fragments (as shown in Figure 2A) and supplied to interact with Rab7 (Figure 2E). The interaction of RILP-3 (307–702 bp) with Rab7 did not result in colonies on the DDO/X culture plates, whereas the RILP-5 (508–903 bp) and RILP-6 (604–1002 bp) groups contained a few colonies. The RILP-0 (1–402 bp), RILP-1 (91–507 bp), RILP-2 (196–603 bp), and RILP-7 (703–1110 bp) groups interacted with Rab7 and formed blue colonies on the QDO/X/A plates. There was no obvious colony on RILP-4 (403–801 bp) and RILP-8 (799–1158 bp) groups. These results suggested that at least two corresponding fragments, 1–400 bp and 700–1110 bp, would participate in the interaction between RILP and Rab7.

The role of RILP-N in the interaction drew our attention, and structural models of Sf-Rab7 and Sf-RILP-N were constructed. The Sf-Rab7 model, which combined GTP and Mg^{2+}, showed higher homology between species and reached a much more stable condition as soon as the model was built (Figure 2F). However, Sf-RILP exhibited an unstable model. Thus, 30-90aa of Sf-RILP-N was selected for the interaction model construction. The Sf-RILP-N model became stable at 30 ns, and the interactional system with Sf-Rab7 showed a similar trend. Although the structure of Sf-RILP-N remained changing, the domain ranging from 30 to 90aa showed a solid combination between the two proteins at 50 ns based on the stable binding position of GTP in Sf-Rab7 (Figure 2G).

E61 at the N-terminus of Sf-RILP was vital for the interaction with Sf-Rab7

According to the stable binding model, H-bonds and salt bridges were marked between Sf-Rab7 and Sf-RILP-N. All the contribution energies of Sf-RILP-N residues (30-90aa) during dynamics simulation were calculated at 20 ns intervals (Figure 3A). Glu61 (E61) showed the highest contribution energy of approximately 50.6752 kJ/mol followed by Glu58 (E58) with 33.0514 kJ/mol. The salt bridges between E61 (Sf-NRILP) and Lys10 (K10, Sf-Rab7) and between E58 (Sf-NRILP) and Arg79 (R79, Sf-Rab7) were considered -potential linkages. Four possible salt bridges were monitored between 0 and 100 ns (Figure 3B). E61-K10

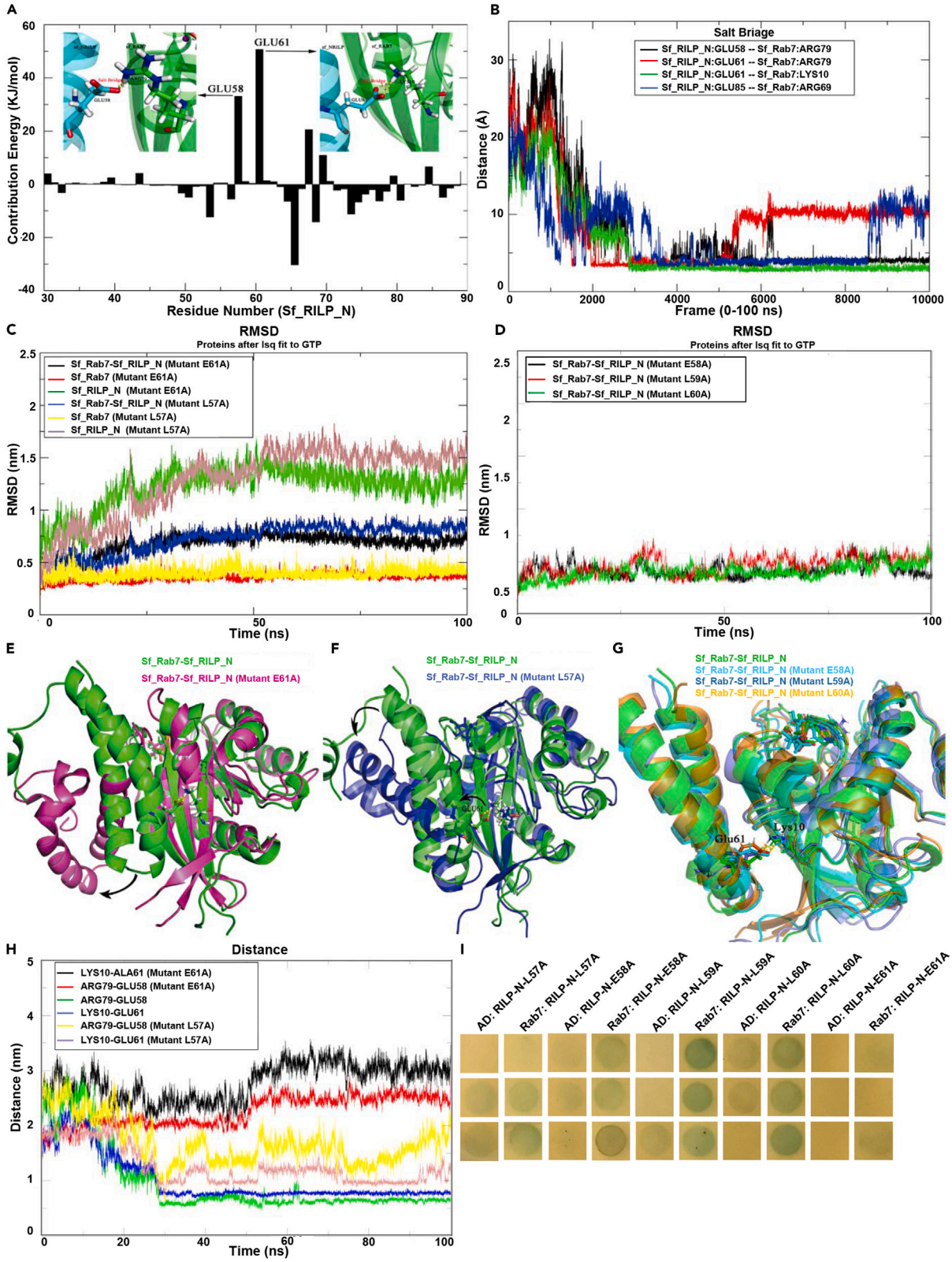
A
GLU61
GLU58
Contribution Energy (KJ/mol)
Residue Number (Sf_RILP_N)
B
Salt Briage
Sf_RILP_N:GLU58 -- Sf_Rab7:ARG79
Sf_RILP_N:GLU61 -- Sf_Rab7:ARG79
Sf_RILP_N:GLU61 -- Sf_Rab7:LYS10
Sf_RILP_N:GLU85 -- Sf_Rab7:ARG69
Distance (Å)
Frame (0-100 ns)
C
RMSD
Proteins after lsq fit to GTP
Sf_Rab7-Sf_RILP_N (Mutant E61A)
Sf_Rab7 (Mutant E61A)
Sf_RILP_N (Mutant E61A)
Sf_Rab7-Sf_RILP_N (Mutant L57A)
Sf_Rab7 (Mutant L57A)
Sf_RILP_N (Mutant L57A)
RMSD (nm)
Time (ns)
D
RMSD
Proteins after lsq fit to GTP
Sf_Rab7-Sf_RILP_N (Mutant E58A)
Sf_Rab7-Sf_RILP_N (Mutant L59A)
Sf_Rab7-Sf_RILP_N (Mutant L60A)
RMSD (nm)
Time (ns)
E
Sf_Rab7-Sf_RILP_N
Sf_Rab7-Sf_RILP_N (Mutant E61A)
F
Sf_Rab7-Sf_RILP_N
Sf_Rab7-Sf_RILP_N (Mutant L57A)
G
Sf_Rab7-Sf_RILP_N
Sf_Rab7-Sf_RILP_N (Mutant E58A)
Sf_Rab7-Sf_RILP_N (Mutant L59A)
Sf_Rab7-Sf_RILP_N (Mutant L60A)
Glu61
Lys10
H
Distance
LYS10-ALA61 (Mutant E61A)
ARG79-GLU58 (Mutant E61A)
ARG79-GLU58
LYS10-GLU61
ARG79-GLU58 (Mutant L57A)
LYS10-GLU61 (Mutant L57A)
Distance (nm)
Time (ns)
I
AD: RILP-N-L57A
Rab7: RILP-N-L57A
AD: RILP-N-E58A
Rab7: RILP-N-E58A
AD: RILP-N-L59A
Rab7: RILP-N-L59A
AD: RILP-N-L60A
Rab7: RILP-N-L60A
AD: RILP-N-E61A
Rab7: RILP-N-E61A

Figure 3. Rab7 K10-RILP E61 was proven to be the key site for Sf-Rab7 recruitment of Sf-RILP-N

(A) The contribution energy of Sf-RILP-N residues (30-90aa) during dynamics simulation.

(B) Analysis of the distances of salt bridges between Sf-Rab7 and Sf-NRILP. E61-K10 (green), E58-R79 (black), E61-R79 (red) and E85-R69 (blue).

(C) Illustration of RMSD on Sf-Rab7 (red and yellow), Sf-RILP-N E61A (green), Sf-RILP-N L57A (green), and their combined system, black for Rab7-E61A and blue for Rab7-L57A.

(D) Illustration of RMSD on the combined system of Sf-Rab7 with E58A (black), L59A (red), and L60A (green).

(E) The binding mode of Sf-RILP-N E61A recruited by Sf-Rab7. Normal interaction is marked with green, and the mutation interaction is purple.

(F) The binding mode of Sf-RILP-N L57A recruited by Sf-Rab7. Normal interactions are marked with green, and mutation interactions are marked with blue.

(G) The binding modes of Sf-RILP-N (green) and Sf-RILP-N E58A (aquamarine), L59A (blue), L60A (orange) recruited by Sf-Rab7.

(H) Analysis of the distances of salt bridges between Sf-Rab7 and Sf-RILP-N E61A and L57A mutations.

(I) Yeast two-hybrid system identified the interaction of the Sf-Rab7 point mutation with five Sf-RILP-N point mutations.

showed a stable salt bridge distance (Å) at approximately 30 ns, whereas E58-R79 was stable at approximately 63 ns. The other two potential linkages, E61-R79 and E85-R69, showed unstable salt bridge distances. It was supposed that E61 of Sf-RILP-N played a vital role during the interaction with Sf-Rab7, whereas E58 might help to consolidate the salt bridge between the two models.

Moreover, the interactional systems of Sf-Rab7 with five Sf-RILP-N mutations, including L57A, E58A, L59A, L60A and E61A, were also tested. The Sf-Rab7 models showed stale conformations at all time intervals. As shown in Figure 3C, both mutations, L57A and E61A, delayed the stable time of Sf-RILP-N, as the L57A model became stable at approximately 50 ns and the E61A model became stable much later. The combined systems showed a similar trend. In particular, the root-mean-square displacement (RMSD) of the E61A combined model decreased slightly after reaching a small platform stage and changed along the time intervals. The stable conformations of the two combined systems are shown in Figures 3E and 3F. The E61A mutation changed the helical structures of Sf-RILP-N dramatically and hampered the interaction with Sf-Rab7. Sf-RILP-N L57 did not interact with Sf-Rab7 directly, but the L57A mutation influenced the interaction of Sf-RILP-N E61 with Sf-Rab7 by changing the space structure. The other three mutations, E58A, L59A and L60A, did not delay the stable time of Sf-RILP-N (Figure 3D). All these stable conformations showed little difference when interacting with Sf-Rab7, and the E61-K10 interaction suffered little influence (Figure 3G). To verify the prediction above, the five amino acid point-mutation sites of Sf-RILP-N were examined for the interaction via yeast two-hybrid systems (Figure 3I). Sf-RILP-N (1–630) could interact with Sf-Rab7 and grow yeast colonies. After point mutation, the L59A and L60A groups appeared colonies on QDO/X/A plates, whereas E61A did not. L57A and E58A influenced the interaction to some extent as the colonies were affected, especially for L57A.

For more information, the distances of the two main salt bridges between Sf-RILP-N and Sf-Rab7, E61-K10 and E58-R79, were analyzed during the mutation systems (Figure 3H). The distance of E61-K10 became stable (0.7 nm) at approximately 30 ns, and that of E58-R79 was approximately 0.6 nm at approximately 30 ns. Mutations of L57A and E61A, especially for E61A, would increase the distances and destroy the salt bridges. However, E58-R79 also plays an important role in the interaction between Rab7 and RILP-N. Thus, E61 became the core amino acid for Sf-RILP-N to interact with Sf-Rab7, and L57 helped to maintain the conformation for the combined system. E61-K10 was vital for the interaction, and E58-R79 was beneficial for keeping the structure stable.

To identify the role of E61-K10, K10 of Rab7 was also replaced with Ala. Rab7K10A did not interact with RILP-1 (91–507 bp), as there were no colonies on the QDO/X/A plates (Figure 4A). However, the interaction of Sf-Rab7 and Sf-RILP-N was not influenced (Figure 4B). No colonies appeared on the DDO/X/A plates of the RILP-N-E61A and Rab7K10A groups, which suggested that there was no interaction between them. The Rab7K10A mutant also influenced the RILP-N-L57A interaction, whereas it did not affect the interaction with other RILP mutants, including RILP-N-E58A, RILP-N-L59A, RILP-N-L60A, and RILP-7 (703–1110 bp).

The corresponding vital amino acids in the mammalian model were neutral in fall armyworm

Specifically, some corresponding verified mutation sites in the human model at Sf-RILP-C, I276A, L277A, R280A and L283A were also examined for the interaction. The interaction between Sf-Rab7 and Sf-RILP-C (631–1158) produced no colonies on DDO/X or QDO/X/A plates, as well as all the point mutated fragments. However, once the GC-rich domain was removed, all the point-mutated regions of Sf-RILP-Cc (604–1110) could interact with Sf-Rab7 (Figure 4C). Moreover, the Rab7K10A mutant did not affect

Figure 4. Vital amino acids in the C-terminus became neutral for the interaction of Sf-RILP and Sf-Rab7, while RILP-N helped the self-interaction in *S. frugiperda* and *D. melanogaster* and biological functions

(A) Yeast two-hybrid systems identified the interaction of Sf-Rab7 and Sf-Rab7K10A with Sf-RILP-1 and Sf-RILP-7.

(B) Yeast two-hybrid systems identified the interaction of Sf-Rab7 and Sf-Rab7K10A with Sf-RILP-N and Sf-RILP- Cc, as well as the related point mutations.

Figure 4. *Continued*

(C) Yeast two-hybrid systems identified the interaction of Sf-Rab7 with Sf-RILP-C and four related point mutations, I276A, L277A, R280A and L283A.

(D) Yeast two-hybrid systems identified the interaction of Sf-Rab7 and Sf-Rab7K10A with Sf-RILP-C and four related point mutations.

(E) Yeast two-hybrid systems identified the interaction of Sf-RILPc, Sf-RILP-Nc, and Sf-RILP-Cc with different RILP terminals on QDO/X/A plates.

(F) Yeast two-hybrid systems identified the interaction between Dm-RILP terminals, DmRI, DmRIc, and DmRN, on QDO/X/A plates.

(G and H) Statistics of ROI mean intensity of Cathepsin L (G) and Atg8 (H) after overexpression of Rab7/RILP in Sf9 cells. D represents the control group with DMSO, and H represents harmine treatment. Significant differences between the control group and harmine treatment were calculated with a t-test (ns, not significant; "*", $p < 0.05$; "**", $p < 0.01$; "***", $p < 0.001$). Different colored lowercase letters indicate significant differences ($p < 0.05$) between different treatments as determined using ANOVA followed by Duncan's multiple range tests.

the interaction of Sf-Rab7 with Sf-RILP-Cc (604–1110) and these mutants (Figure 4D). Thus, the C-terminus of RILP would show different inaction sites among humans and insects.

RILP terminals helped the self-interaction in *S. frugiperda* and *D. melanogaster*

As the Rab7 binding region of RILP (244-308aa) formed a coiled-coil homodimer in a human model,[12] the interaction between Sf-RILP fragments was also detected. Sf-RILPc could interact with both the N- and C-termini of Sf-RILP (Figure 4D), whereas its interaction with Sf-RILP and Sf-RILPc in a weaker manner, especially for the homodimer of Sf-RILPc, only showed colonies on triple dropout media containing X-α-Gal and aureobasidin A (TDO/X/A) plates (Figure S12). The same phenomenon appeared for Sf-RILP-Nc and Sf-RILP-Cc, which showed that Sf-RILP-Nc interacted with all RILP fragments and that Sf-RILP-Cc could also interact with Sf-RILP-Nc, as well as itself. All these forms of self-interaction made the model more complex.

Although the interaction between Rab7 and RILP in *Drosophila* has not been reported, self-interactions between Dm-RILP fragments were observed (Figure 4F). Both DmRIc and DmRN could form stable homodimers, as there were obvious blue colonies on QDO/X/A plates, while there was only a weaker interaction between DmRI fragments (Figure S12). More importantly, DmRN was sufficient to interact with DmRI and DmRIc, which emphasized the role of the N-terminus in self-interaction. In total, the Rab7-RILP interaction showed differences between fall army worms and fruit flies, and it might display a special species complexity accompanied by evolutionary selection.

RILP terminals participated in the autophagy progress of Sf9 cells

In addition, according to our recent studies, harmine, the main compound of many traditional medicines, exhibited stronger autophagy induction effects on insect *Spodoptera frugiperda* Sf9 cells.[22–24] Thus, the roles of Sf-Rab7 and Sf-RILP terminals on lysosome and autophagy were investigated in Sf9 cells with overexpression and RNA interference (RNAi).

The Sf9 cells emitted green fluorescence after transfer with the insect expression vector PIZT-V5/His (PIZT, Figure S13). Cathepsin L, an important lysosomal enzyme, and Atg8, a typical compound of autophagic membrane, were marked with Cyanine 3 (CY3)-labeled secondary antibodies. The ROI (region of interest) mean intensity of red fluorescence within the gene over-expressed cells (marked with green fluorescence, intensity ≥ 50) were evaluated (Figures 4G and 4H). Overexpression of *Sf-Rab7*, the inactivated Rab7 mutant *Sf-Rab7T22N*, and N-terminus of Sf-RILP (*Sf-RILP-N*) had little effect on the expression of Cathepsin L, whereas overexpression of *Sf-RILP* and the C-terminus of *Sf-RILP* (*Sf-RILP-C*) might contribute to the accumulation of Cathepsin L in cells, especially accompanied by harmine treatment. Moreover, harmine treatment increased the expression of Atg8 in all the groups as autophagy was induced. But only overexpression of *Sf-RILP-N* showed a significant increase on both DMSO and harmine treatment, whereas overexpression of *Sf-Rab7* and *Sf-Rab7T22N* seemed to alleviate the increase. Furthermore, the roles of mutations on Sf-RILP-N were also detected after overexpression (Figures S14 and S15). The expression of Atg8 in overexpressed cells of *Sf-RILP-N-L59A* and *Sf-RILP-N-L60A* increased significantly at both DMSO and harmine treatment. However, it only exhibited a few difference with control groups on the *Sf-RILP-N-E61A* overexpression group (Figures 5A and 5B). As for the expression of Cathepsin L, it related to the treatments, DMSO or harmine, rather than mutations of Sf-RILP-N (Figure 5C). These results suggested the role of RILP-N and E61 on the autophagy procedure.

The RNAi system was established (Figure S16), and immunofluorescence of Cathepsin L and Atg8 was performed simultaneously (Figure 5D and Figure S17). Area, mean diameter, mean density, and IOD

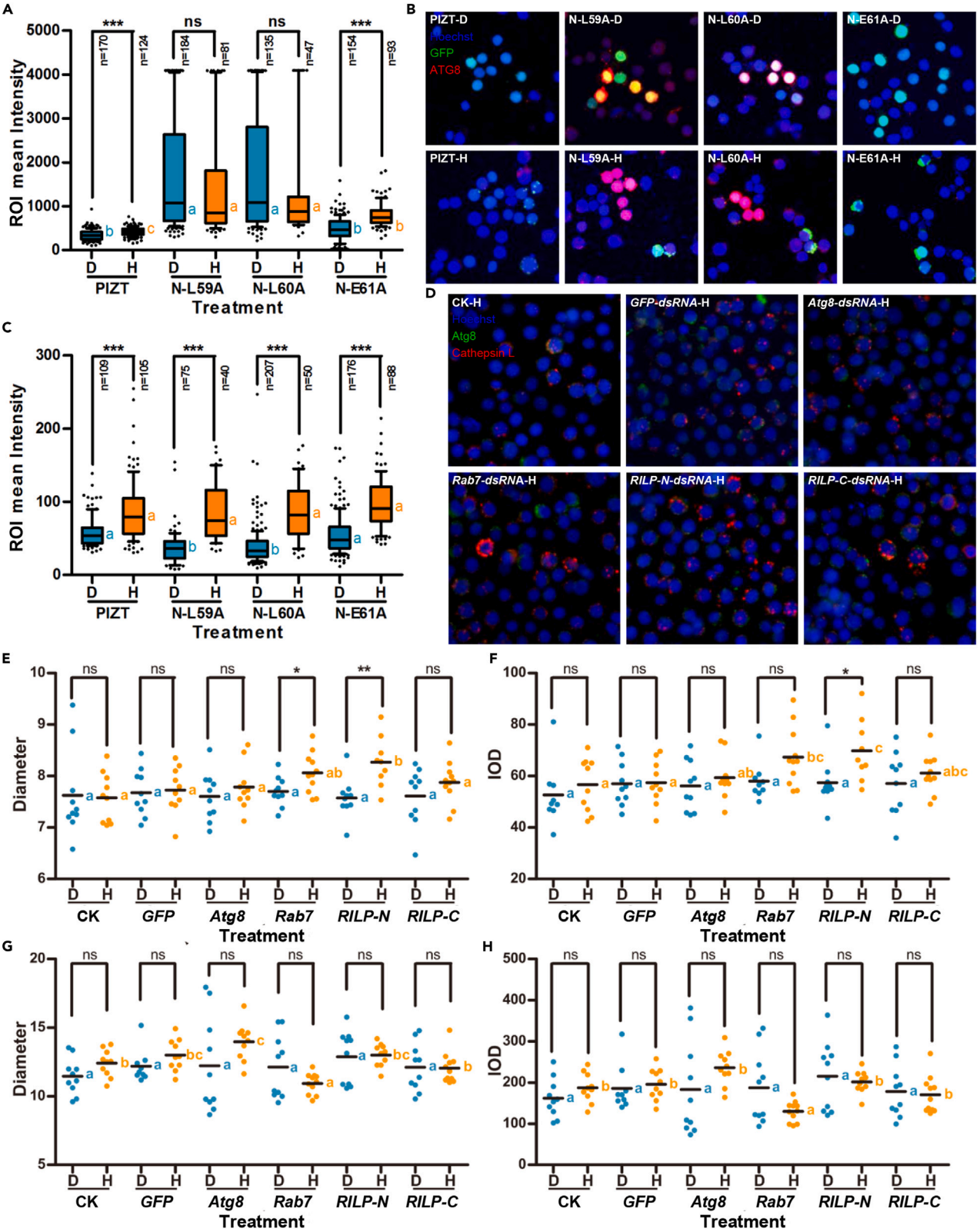
A
ROI mean Intensity
Treatment
PIZT
N-L59A
N-L60A
N-E61A
B
PIZT-D
Hoechst
GFP
ATG8
N-L59A-D
N-L60A-D
N-E61A-D
PIZT-H
N-L59A-H
N-L60A-H
N-E61A-H
C
ROI mean Intensity
Treatment
D
CK-H
Hoechst
Atg8
Cathepsin L
GFP-dsRNA-H
Atg8-dsRNA-H
Rab7-dsRNA-H
RILP-N-dsRNA-H
RILP-C-dsRNA-H
E
Diameter
CK
GFP
Atg8
Rab7
RILP-N
RILP-C
Treatment
F
IOD
Treatment
G
Diameter
Treatment
H
IOD
Treatment

Figure 5. RILP terminals participated in the autophagy progress of Sf9 cells

(A) Statistics of ROI mean intensity of Atg8 after overexpression of mutations of RILP-N in Sf9 cells.

(B) Colocalization of GFP and Atg8 after overexpression of mutations of RILP-N in Sf9 cells.

(C) Statistics of ROI mean intensity of Cathepsin L after overexpression of mutations of RILP-N in Sf9 cells.

(D) Colocalization of Cathepsin L and Atg8 after RNAi of Rab7/RILP in Sf9 cells with harmine treatment.

(E and F) Statistics of diameter (E) and IOD (F) of Cathepsin L-positive points after RNAi of Rab7/RILP in Sf9 cells.

(G and H) Statistics of diameter (G) and IOD (H) of Atg8-positive points after RNAi of Rab7/RILP in Sf9 cells. PIZT, PIZT-V5/His; N-L59A, Sf-RILP-N-L59A-PIZT; N-L60A, Sf-RILP-N-L60A-PIZT; N-E61A, Sf-RILP-N-E61A-PIZT; D represents the control group with DMSO, and H represents harmine treatment. Significant differences between the control group and harmine treatment were calculated with a *t-test* (ns, not significant; "*", $p < 0.05$; "**", $p < 0.01$; "***", $p < 0.001$). Different colored lowercase letters indicate significant differences ($p < 0.05$) between different treatments as determined using ANOVA followed by Duncan's multiple range tests.

(Integrated Optical Density) of positive points (Cathepsin L intensity ≥15, Atg8 intensity ≥20) were calculated (Figures 5E–5H and S18). The statistics of area and mean diameter exhibited similar trend to reveal the shape of positive points, as well as the mean density and IOD, revealing the intensity. The results showed that transfecting dsRNA of *Rab7*, *RILP-N* and *RILP-C* might increase the diameter and IOD of Cathepsin L, suggesting the enlarged lysosomes with strong activity. Among them, RNAi of *RILP-N* showed the significantly enhanced Cathepsin L-positive points, followed by the RNAi of *Rab7* and *RILP-C*. As for Atg8, RNAi of *Rab7*, *RILP-N* and *RILP-C* seemed to decrease the Atg8-positive points, especially after transfection with dsRNA of *Rab7*. In brief, the results of overexpression and RNAi demonstrated the role of Sf-Rab7 and Sf-RILP during insect autophagolysosomal maturation, and Sf-RILP-N seemed to play a unique role during the autophagy procedure.

DISCUSSION

Rab proteins are essential for membrane fusion and vesicular transport in mammalian cells, and RILP interacts with active Rab7 to recruit functional dynein-dynactin motor complexes to late endosomes and lysosomes, as well as other intracellular membrane compartments.[5,25,26] RILP recruits dynein–dynactin motors on Rab7-GTP-positive phagosomes, and the recruitment not only displaces phagosomes centripetally but also promotes the extension of phagosomal tubules toward late endocytic compartments. RILP is therefore a key protein for the biogenesis of lysosomes and phagolysosomes. The Rab7-RILP-dynein motor cascade has been shown to act on autophagic vacuoles, Salmonella-containing phagosomes, early melanosomes, major histocompatibility complex class II-containing compartments, and cytolytic granules.[5–7,26,27] Overexpression of RILP induced late endosome/lysosome enlargement and clustering to the perinuclear region, whereas depletion of RILP strongly impaired endosomal maturation as well as phagosome fusion to lysosomes.[18,19] RILP can also interact with other Rabs, ATPase, ESCRT complex, HOPS subunits and autophagic proteins during various life procedures. For example, RILP could interact with the GTP-bound forms Rab34 and Rab36 in the C-terminal region (aa199-401) independently of Rab7.[28,29] RILP is also reported to interact with insulin granule-associated Rab26 to restrict insulin secretion,[30] and the CC2-containing domains in the C-terminus of RILP mediate Rab12 binding to regulate retrograde transport of mast cell secretory granules.[31] Except for Rab proteins, RILP can simultaneously control endosome acidification and translocation toward the microtubule organizing center by directly interacting with V1G1 (ATP6V1G1).[32] More importantly, the N-terminus and C-terminus of RILP interact with VPS22 and VPS36 of ESCRT-II, respectively, to regulate their membrane recruitment during the endocytic pathway.[33] Two HOPS subunits, VPS18 and VPS41, exhibit low affinity for Rab7 alone but much higher affinity for RILP and Rab7-RILP interactions.[34] Recently, RILP was proven to control the neuronal autophagy pathway through sequential interactions with Atg5, Atg8/LC3, Rab7, and dynein to regulate autophagosome formation, transport, and turnover in a mTOR-responsive mechanism.[35,36] The depletion of RILP promoted the cell proliferation and migration of breast and prostate cancer cell lines, which linked RILP with human cancers and diseases.[37] Thus, RILP plays a vital role during vesicular transport in multicellular organisms, and clarifying its related interactions would help to explore its vital functions.

However, RILP appears to be poorly conserved evolutionarily, and no extensive homology is found with any known yeast protein (Figure 6A). In view of the fact that these unicellular organisms have only few but large vacuoles, they might not need RILP, which apparently serves to induce fewer but larger lysosomes.[38] RILP function developed late in evolution and is probably related to the increasing complexity of vesicular transport in higher eukaryotes.[39] In insects, there are a few reports on the biochemical and cellular functions of RILP. For example, CG11448 is the single Drosophila ortholog of mammalian RILP and its two paralogs, RILPL1 and RILPL2 (Figure 6B). However, the unique region for RILP to bind Rab7 is missing from both

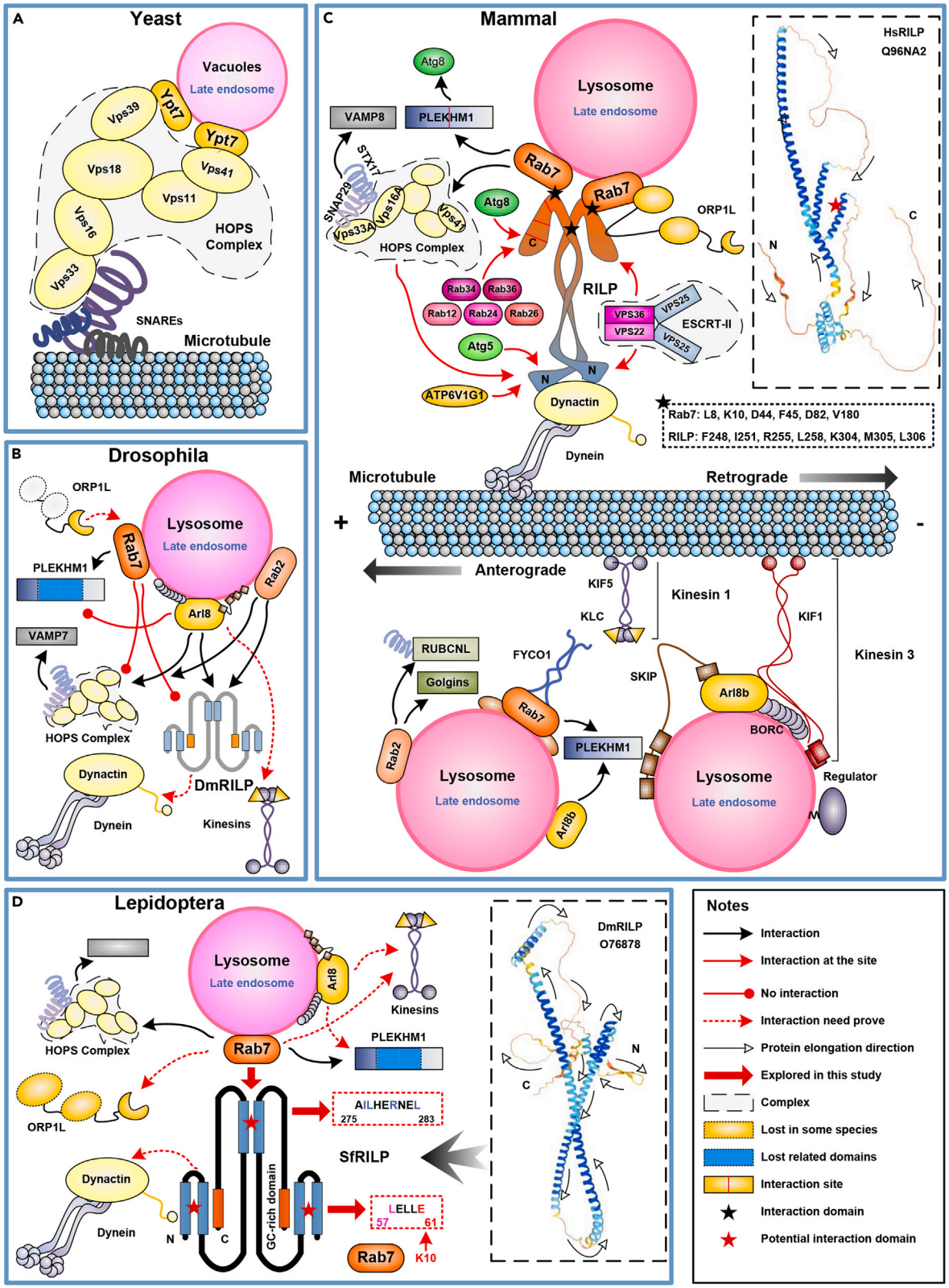
A
Yeast
Vacuoles
Late endosome
Ypt7
Ypt7
Vps39
Vps18
Vps41
Vps11
Vps16
Vps33
HOPS Complex
SNAREs
Microtubule
B
Drosophila
ORP1L
Lysosome
Late endosome
Rab7
Rab2
Arl8
PLEKHM1
VAMP7
HOPS Complex
Dynactin
DmRILP
Dynein
Kinesins
C
Mammal
Atg8
Lysosome
Late endosome
VAMP8
PLEKHM1
STX17
SNAP29
Vps16A
Vps33A
Vps41
HOPS Complex
Rab7
Rab7
ORP1L
Atg8
C
Rab34
Rab36
Rab12
Rab24
Rab26
RILP
VPS36
VPS22
VPS25
VPS25
ESCRT-II
Atg5
N
N
ATP6V1G1
Dynactin
Dynein
HsRILP
Q96NA2
C
N
Rab7: L8, K10, D44, F45, D82, V180
RILP: F248, I251, R255, L258, K304, M305, L306
Microtubule
Retrograde
+
-
Anterograde
KIF5
KLC
Kinesin 1
KIF1
Kinesin 3
RUBCNL
Golgins
FYCO1
SKIP
Arl8b
BORC
Rab7
Rab2
PLEKHM1
Lysosome
Late endosome
Lysosome
Late endosome
Arl8b
Regulator
D
Lepidoptera
Lysosome
Late endosome
Arl8
Kinesins
HOPS Complex
Rab7
PLEKHM1
ORP1L
AILHERNEL
275
283
SfRILP
Dynactin
Dynein
N
C
GC-rich domain
LELLE
57
61
Rab7
K10
DmRILP
O76878
N
C
Notes
Interaction
Interaction at the site
No interaction
Interaction need prove
Protein elongation direction
Explored in this study
Complex
Lost in some species
Lost related domains
Interaction site
Interaction domain
Potential interaction domain

Figure 6. Evolutional insights into the Rab7-RILP interaction-related mechanism of lysosome motility

(A) In yeast, Ypt7 is present on the membranes of vacuoles and late endosomes, where the HOPS complex connects the membranes through SNARE proteins. This pattern is largely true in Drosophila, Lepidoptera and mammals.

(B) In Drosophila, Rab7 cannot interact with HOPS subunits and the sole RILP homolog, while Arl8 and Rab2 are proven to substitute for its roles. Many compounds or key domains of Rab7 effectors, including RILP, FYCO1, PLEKHM1 and ORP1L, are absent from insect systems.

(C) In mammals, Arl8b-BORC-SKIP-induced anterograde movement via kinesins and Rab7-mediated bidirectional translocation though various effectors make the system more complex. Rab7-GTP recruits RILP (at the C-terminus) and ORP1L, and then directly interacts with dynactin subunit 1 ($p150^{Glued}$) of the transporter dynein-dynactin at the N-terminus of RILP. Finally, dynein initiates translocation of late endosome or lysosome to the end of microtubules. Moreover, Rab7 could also interact with FYCO1 to mediate anterograde movement via kinesins and interact with Atg8 and the HOPS complex through PLEKHM1. RILP also plays various roles by interacting with many other factors, including Rabs, ATPase, Atgs, the HOPS complex and the ESCRT-II complex.

(D) In Lepidoptera, Sf-Rab7 is supposed to interact with Sf-RILP through both the N-terminal and C-terminal, in which E61-K10 in the N-terminal play vital roles and the corresponding proven amino acids in the C-terminal play a neutral influence. A potential interaction model was proposed based on the space structures of Hs-RILP (Q96NA2) and Dm-RILP (O76878). RILP forms a homodimer within its C-terminus and interacts with two independent Rab7-GTPs in Lepidoptera, whereas the coiled-coil region in the N-terminus also interacts with one or two Rab7-GTP residues once the GC-rich domain is removed from the C-terminus. A similar situation might occur in Drosophila, except that Rab7 is replaced by Alr8 or Rab2.

human RILPL1/2 and Drosophila CG11448, whereas the $p150^{Glued}$-binding region is well conserved in both RILPL1 and CG11448.[20] CG11448 is supposed to interact with Arl8 directly but not Rab7 in Drosophila, although this would not preclude CG11448 from binding HOPS. However, human Arl8b-positive lysosomes did not show detectable enrichment of RILP family members. Moreover, there is no strong interaction between Drosophila Rab7 and Vps39/Vps41 or the sole fly RILP ortholog.[40] Drosophila Rab2, rather than Rab7, has been proven to play roles in late endosome-lysosome fusion and autophagosome-lysosome fusion in a HOPS-dependent manner.[21,41] Here, in our reports, the interaction mechanism between Rab7 and RILP in fruit flies was also explored. The results were in accordance with previous conclusions that there was no interaction between Rab7 and whole length RILP, GC-rich domain removed RILP, or N-terminal parts. However, RILP of *S. frugiperda* could also interact with Rab7 to participate in lysosome transport, although in a novel manner, removing the GC-rich domain in the C-terminal and combining with the N-terminal and potentially involving C-terminal segments. Thus, the Rab7-RILP interaction was not vertebrate-specific but a feature of highly evolved creatures, whereas lepidopteran insects showed the highest similarity with mammals or vertebrates. It is interesting to find that terminals and fragments of RILP could form homodimers or heterodimers in both Drosophila and *S. frugiperda*, which made the interaction of RILP among species more unique and complex.

The Rab7-RILP interaction is well described in the human model (Figure 6C).[12,13,18,42,43] There are two Rab7-specific interaction regions within RILP, one involving the transition and interconversion regions and the second containing RabSF1 and RabSF4. Point mutations, such as L8A, K10A, D44A, F45A, D82A, and V180A, could disrupt the interaction of Rab7 and RILP, eliminating the movement of Rab7 and RILP to late endosomes/lysosomes.[12] For RILP, the C-terminal half is proven to interact with GTP-Rab7, and the N-terminal half is supposed to interact with the C-terminal 25-kD fragment of $p150^{Glued}$ and with the C-terminus of ORP1L.[13] The Rab7 binding region of RILP (244-308aa) forms a coiled-coil homodimer with two symmetry surfaces, interacting with two separated Rab7-GTP molecules to form a dyad configuration of Rab7-RILP(2)-Rab7. Point mutations, such as F248A, I251A, R255A, L258A, K304A, M305A, and L306A, disrupt RILP dimerization and eliminate its binding to Rab7-GTP and to late endosomes/lysosomes.[12] However, in the article, the N-termini were necessary to interact with Rab7, which was identified with a yeast two-hybrid system, GST pull-down and model construction (Figure 6D). Two potential interaction segments, 1–300 bp and 700–1100 bp, corresponded to the N- and C-termini without the GC-rich domain. Moreover, E61 and L57 were supposed to be important for the Rab7-RILP interaction, whereas other selected amino acids from the N- and C-termini (E58, L59, L60, I276, L277, R280 and L283) did not influence the interaction with alanine substitutions. E61 of RILP-N constructed a strong salt bridge with K10 of Rab7, whereas L57 helped to maintain the spatial structure for the bond. We noted that K10 of Rab7 had already been proven to affect the connection of Rab7 with RILP (244-308aa) in human models.[12] However, it interacted with the N-terminal E61 rather than the C-terminal in the insect model. Thus, these results suggested a distinct Rab7-RILP interaction in insects. In our hypothesis, one insect RILP might connect with two independent Rab7 through both terminals, and the structural basis would become more complex when considering RILP dimerization and interaction with dynactin subunits, which requires much more effort to obtain more details of the complex system in invertebrate physiology.

In conclusion, the less conserved RILP exhibited a novel interaction with Rab7 during the lysosome motility of insects. The N-terminus of RILP were proven to be necessary for the interaction, and a GC-rich domain in

the C-terminus was supposed to hamper the interaction. The verified binding sites in the C-terminus of mammalian RILP were neutral in insects, whereas Glu61 in the N-terminus of insect RILP was supposed to be the key amino acid, and Leu57 helped to maintain the conformation for the interaction. Both termini, especially the N-terminus, exhibited important roles during the autophagy procedure and RILP dimerization. The different interaction modes of Rab7-RILP shed light on the physiological functions of species-specific mechanisms and enrich the evolutionary knowledge of the complex systems of vesicle transport in multicellular organisms.

Limitations of the study

This study had some limitations. First, the expressed proteins, RILPc-His and RILP-Cc-His, could not be purified from the supernatants, leading their crude proteins could not interact with Rab7 in the recently GST pull-down assay. Second, the C-terminus of insect RILP would help for the interaction, but the key points have not been proved. Third, the detailed interaction manner of insect Rab7-RILP have not been proposed and verified since the complex mechanism.

STAR★METHODS

Detailed methods are provided in the online version of this paper and include the following:

- KEY RESOURCES TABLE
- RESOURCE AVAILABILITY
  - Lead contact
  - Materials availability
  - Data and code availability
- EXPERIMENTAL MODEL AND STUDY PARTICIPANT DETAILS
  - Cell lines
- METHOD DETAILS
  - Bioinformatics analysis
  - Point mutations and truncated expression
  - Yeast two-hybrid system
  - GST pull-down assay
  - Model construction
  - Dynamic optimization of Sf-RILP-N
  - Docking simulation of Sf-Rab7 and Sf-NRILP
  - Dynamic monitoring of the recruiting process
  - Binding energy calculation
  - Overexpression of Rab7 and RILP
  - RNA interference of Rab7 and RILP
- QUANTIFICATION AND STATISTICAL ANALYSIS

SUPPLEMENTAL INFORMATION

Supplemental information can be found online at https://doi.org/10.1016/j.isci.2023.107040.

ACKNOWLEDGMENTS

This research was funded by National Natural Science Foundation of China (No. 32000342), Chinese Postdoctoral Science Foundation (No. 2020M672650), and the National Key Research and Development Program of China (No. 2018YFD0200300). The funders had no role in study design, data collection and analysis, decision to publish, or preparation of the manuscript.

AUTHOR CONTRIBUTIONS

Conceptualization, G.C. and G.Z.; Formal Analysis, G.C., Z.J., and Y.C.; Software, Z.J.; Data curation, Y.L.; Validation, Y.C. and Y.L.; Investigation, S.A. and R.S.; Resources, S.A. and R.S.; Supervision, Y.X. and G.Z.; Writing – original draft, G.C.; Writing – review and editing, Y.X. and G.Z.; Funding acquisition, G.C. and G.Z.; Project administration, G.C. and G.Z.

DECLARATION OF INTERESTS

The authors declare no competing interests.

Received: February 21, 2022
Revised: December 12, 2022
Accepted: June 1, 2023
Published: June 7, 2023

REFERENCES

1. Lie, P.P.Y., and Nixon, R.A. (2019). Lysosome trafficking and signaling in health and neurodegenerative diseases. Neurobiol. Dis. *122*, 94–105. https://doi.org/10.1016/j.nbd.2018.05.015.

2. Ballabio, A., and Bonifacino, J.S. (2020). Lysosomes as dynamic regulators of cell and organismal homeostasis. Nat. Rev. Mol. Cell Biol. *21*, 101–118. https://doi.org/10.1038/s41580-019-0185-4.

3. Johnson, D.E., Ostrowski, P., Jaumouillé, V., and Grinstein, S. (2016). The position of lysosomes within the cell determines their luminal pH. J. Cell Biol. *212*, 677–692. https://doi.org/10.1083/jcb.201507112.

4. Levine, B., and Kroemer, G. (2019). Biological functions of autophagy genes: a disease perspective. Cell *176*, 11–42. https://doi.org/10.1016/j.cell.2018.09.048.

5. Stroupe, C. (2018). This is the end: regulation of Rab7 nucleotide binding in endolysosomal trafficking and autophagy. Front. Cell Dev. Biol. *6*, 129. https://doi.org/10.3389/fcell.2018.00129.

6. Guerra, F., Paiano, A., Migoni, D., Girolimetti, G., Perrone, A.M., De Iaco, P., Fanizzi, F.P., Gasparre, G., and Bucci, C. (2019). Modulation of RAB7A protein expression determines resistance to cisplatin through late endocytic pathway impairment and extracellular vesicular secretion. Cancers *11*, 52. https://doi.org/10.3390/cancers11010052.

7. Roque, N.R., Lage, S.L., Navarro, R., Fazolini, N., Maya-Monteiro, C.M., Rietdorf, J., Melo, R.C.N., D'Avila, H., and Bozza, P.T. (2020). Rab7 controls lipid droplet-phagosome association during mycobacterial infection. BBA-Mol. Cell Biol. L. *1865*, 158703. https://doi.org/10.1016/j.bbalip.2020.158703.

8. Szatmári, Z., and Sass, M. (2014). The autophagic roles of Rab small GTPases and their upstream regulators: a review. Autophagy *10*, 1154–1166. https://doi.org/10.4161/auto.29395.

9. Guerra, F., and Bucci, C. (2016). Multiple roles of the small GTPase Rab7. Cells *5*, 34. https://doi.org/10.3390/cells5030034.

10. Khatter, D., Raina, V.B., Dwivedi, D., Sindhwani, A., Bahl, S., and Sharma, M. (2015). The small GTPase Arl8b regulates assembly of the mammalian HOPS complex on lysosomes. J. Cell Sci. *128*, 1746–1761. https://doi.org/10.1242/jcs.162651.

11. Jongsma, M.L., Bakker, J., Cabukusta, B., Liv, N., van Elsland, D., Fermie, J., Akkermans, J.L., Kuijl, C., van der Zanden, S.Y., Janssen, L., et al. (2020). SKIP-HOPS recruits TBC1D15 for a Rab7-to-Arl8b identity switch to control late endosome transport. EMBO J. *39*, e102301. https://doi.org/10.15252/embj.2019102301.

12. Wu, M., Wang, T., Loh, E., Hong, W., and Song, H. (2005). Structural basis for recruitment of RILP by small GTPase Rab7. EMBO J. *24*, 1491–1501. https://doi.org/10.1038/sj.emboj.7600643.

13. Johansson, M., Rocha, N., Zwart, W., Jordens, I., Janssen, L., Kuijl, C., Olkkonen, V.M., and Neefjes, J. (2007). Activation of endosomal dynein motors by stepwise assembly of Rab7-RILP-p150^{Glued}, ORP1L, and the receptor βIII spectrin. J. Cell Biol. *176*, 459–471. https://doi.org/10.1083/jcb.200606077.

14. Pankiv, S., Alemu, E.A., Brech, A., Bruun, J.A., Lamark, T., Overvatn, A., Bjørkøy, G., and Johansen, T. (2010). FYCO1 is a Rab7 effector that binds to LC3 and PI3P to mediate microtubule plus end-directed vesicle transport. J. Cell Biol. *188*, 253–269. https://doi.org/10.1083/jcb.200907015.

15. Scherer, J., Yi, J., and Vallee, R.B. (2020). Role of cytoplasmic dynein and kinesins in adenovirus transport. FEBS Lett. *594*, 1838–1847. https://doi.org/10.1002/1873-3468.13777.

16. Willson, J. (2020). RILP gets cleaved and exosomes leave. Nat. Rev. Mol. Cell Biol. *21*, 658–659. https://doi.org/10.1038/s41580-020-00299-6.

17. McEwan, D.G., Popovic, D., Gubas, A., Terawaki, S., Suzuki, H., Stadel, D., Coxon, F.P., Miranda de Stegmann, D., Bhogaraju, S., Maddi, K., et al. (2015). PLEKHM1 regulates autophagosome-lysosome fusion through HOPS complex and LC3/GABARAP proteins. Mol. Cell. *57*, 39–54. https://doi.org/10.1016/j.molcel.2014.11.006.

18. Cantalupo, G., Alifano, P., Roberti, V., Bruni, C.B., and Bucci, C. (2001). Rab-interacting lysosomal protein, RILP: the Rab7 effector required for transport to lysosomes. EMBO J. *20*, 683–693. https://doi.org/10.1093/emboj/20.4.683.

19. Jordens, I., Fernandez-Borja, M., Marsman, M., Dusseljee, S., Janssen, L., Calafat, J., Janssen, H., Wubbolts, R., and Neefjes, J. (2001). The Rab7 effector protein RILP controls lysosomal transport by inducing the recruitment of dynein-dynactin motors. Curr. Biol. *11*, 1680–1685. https://doi.org/10.1016/s0960-9822(01)00531-0.

20. Rosa-Ferreira, C., Sweeney, S.T., and Munro, S. (2018). The small G protein Arl8 contributes to lysosomal function and long-range axonal transport in *Drosophila*. Biol. Open *7*, bio035964. https://doi.org/10.1242/bio.035964.

21. Lund, V.K., Madsen, K.L., and Kjaerulff, O. (2018). Drosophila Rab2 controls endosome-lysosome fusion and LAMP delivery to late endosomes. Autophagy *14*, 1520–1542. https://doi.org/10.1080/15548627.2018.1458170.

22. Cui, G., Shu, B., Veeran, S., Yuan, H., Yi, X., and Zhong, G. (2019). Natural β-carboline alkaloids regulate the PI3K/Akt/mTOR pathway and induce autophagy in insect Sf9 cells. Pestic. Biochem. Physiol. *154*, 67–77. https://doi.org/10.1016/j.pestbp.2018.12.005.

23. Cui, G., Sun, R., Veeran, S., Shu, B., Yuan, H., and Zhong, G. (2020). Combined transcriptomic and proteomic analysis of harmine on *Spodoptera frugiperda* Sf9 cells to reveal the potential resistance mechanism. J. Proteonomics *211*, 103573. https://doi.org/10.1016/j.jprot.2019.103573.

24. Cui, G., Yuan, H., Jiang, Z., Zhang, J., Sun, Z., and Zhong, G. (2020). Natural harmine negatively regulates the developmental signaling network of *Drosophila melanogaster*, Drosophilidae: Diptera *in vivo*. Ecotoxicol. Environ. Saf. *190*, 110134. https://doi.org/10.1016/j.ecoenv.2019.110134.

25. Marwaha, R., Arya, S.B., Jagga, D., Kaur, H., Tuli, A., and Sharma, M. (2017). The Rab7 effector PLEKHM1 binds Arl8b to promote cargo traffic to lysosomes. J. Cell Biol. *216*, 1051–1070. https://doi.org/10.1083/jcb.201607085.

26. Tan, E.H.N., and Tang, B.L. (2019). Rab7a and mitophagosome formation. Cells *8*, 224. https://doi.org/10.3390/cells8030224.

27. Wang, G., Hu, H.B., Chang, Y., Huang, Y., Song, Z.Q., Zhou, S.B., Chen, L., Zhang, Y.C., Wu, M., Tu, H.Q., et al. (2019). Rab7 regulates primary cilia disassembly through cilia excision. J. Cell Biol. *218*, 4030–4041. https://doi.org/10.1083/jcb.201811136.

28. Wang, T., and Hong, W. (2005). Assay and functional properties of Rab34 interaction with RILP in lysosome morphogenesis. Methods Enzymol. *403*, 675–687. https://doi.org/10.1016/S0076-6879(05)03058-2.

29. Chen, L., Hu, J., Yun, Y., and Wang, T. (2010). Rab36 regulates the spatial distribution of late endosomes and lysosomes through a similar mechanism to Rab34. Mol. Membr. Biol. *27*, 23–30. https://doi.org/10.3109/09687680903417470.

30. Zhou, Y., Liu, Z., Zhang, S., Zhuang, R., Liu, H., Liu, X., Qiu, X., Zhang, M., Zheng, Y., Li, L., et al. (2020). RILP restricts insulin secretion through mediating lysosomal degradation of proinsulin. Diabetes *69*, 67–82. https://doi.org/10.2337/db19-0086.

31. Efergan, A., Azouz, N.P., Klein, O., Noguchi, K., Rothenberg, M.E., Fukuda, M., and Sagi-Eisenberg, R. (2016). Rab12 regulates retrograde transport of mast cell secretory granules by interacting with the RILP-Dynein complex. J. Immunol. *196*, 1091–1101. https://doi.org/10.4049/jimmunol.1500731.

32. De Luca, M., Cogli, L., Progida, C., Nisi, V., Pascolutti, R., Sigismund, S., Di Fiore, P.P., and Bucci, C. (2014). RILP regulates vacuolar ATPase through interaction with the V1G1 subunit. J. Cell Sci. *127*, 2697–2708. https://doi.org/10.1242/jcs.142604.

33. Wang, T., and Hong, W. (2006). RILP interacts with VPS22 and VPS36 of ESCRT-II and regulates their membrane recruitment. Biochem. Bioph. Res. Co. *350*, 413–423. https://doi.org/10.1016/j.bbrc.2006.09.064.

34. Lin, X., Yang, T., Wang, S., Wang, Z., Yun, Y., Sun, L., Zhou, Y., Xu, X., Akazawa, C., Hong, W., and Wang, T. (2014). RILP interacts with HOPS complex via VPS41 subunit to regulate endocytic trafficking. Sci. Rep. *4*, 7282. https://doi.org/10.1038/srep07282.

35. Khobrekar, N.V., Quintremil, S., Dantas, T.J., and Vallee, R.B. (2020). The dynein adaptor RILP controls neuronal autophagosome biogenesis, transport, and clearance. Dev. Cell *53*, 141–153.e4. https://doi.org/10.1016/j.devcel.2020.03.011.

36. Khobrekar, N.V., and Vallee, R.B. (2020). A RILP-regulated pathway coordinating autophagosome biogenesis with transport. Autophagy *16*, 1537–1538. https://doi.org/10.1080/15548627.2020.1778294.

37. Lin, J., Zhuo, Y., Yin, Y., Qiu, L., Li, X., and Lai, F. (2021). Methylation of RILP in lung cancer promotes tumor cell proliferation and invasion. Mol. Cell. Biochem. *476*, 853–861. https://doi.org/10.1007/s11010-020-03950-0.

38. Bröcker, C., Kuhlee, A., Gatsogiannis, C., Balderhaar, H.J.k., Hönscher, C., Engelbrecht-Vandré, S., Ungermann, C., and Raunser, S. (2012). Molecular architecture of the multisubunit homotypic fusion and vacuole protein sorting, HOPS tethering complex. Proc. Natl. Acad. Sci. USA *109*, 1991–1996. https://doi.org/10.1073/pnas.1117797109.

39. Wickner, W. (2010). Membrane fusion: five lipids, four SNAREs, three chaperones, two nucleotides, and a Rab, all dancing in a ring on yeast vacuoles. Annu. Rev. Cell Dev. Biol. *26*, 115–136. https://doi.org/10.1146/annurev-cellbio-100109-104131.

40. Gillingham, A.K., Sinka, R., Torres, I.L., Lilley, K.S., and Munro, S. (2014). Toward a comprehensive map of the effectors of Rab GTPases. Dev. Cell *31*, 358–373. https://doi.org/10.1016/j.devcel.2014.10.007.

41. Ding, X., Jiang, X., Tian, R., Zhao, P., Li, L., Wang, X., Chen, S., Zhu, Y., Mei, M., Bao, S., et al. (2019). RAB2 regulates the formation of autophagosome and autolysosome in mammalian cells. Autophagy *15*, 1774–1786. https://doi.org/10.1080/15548627.2019.1596478.

42. Wang, T., Wong, K.K., and Hong, W. (2004). A unique region of RILP distinguishes it from its related proteins in its regulation of lysosomal morphology and interaction with Rab7 and Rab34. Mol. Biol. Cell *15*, 815–826. https://doi.org/10.1091/mbc.E03-06-0413.

43. van der Kant, R., Fish, A., Janssen, L., Janssen, H., Krom, S., Ho, N., Brummelkamp, T., Carette, J., Rocha, N., and Neefjes, J. (2013). Late endosomal transport and tethering are coupled processes controlled by RILP and the cholesterol sensor ORP1L. J. Cell Sci. *126*, 3462–3474. https://doi.org/10.1242/jcs.129270.

44. Chen, C., Chen, H., Zhang, Y., Thomas, H.R., Frank, M.H., He, Y., and Xia, R. (2020). TBtools: an integrative toolkit developed for interactive analyses of big biological data. Mol. Plant *13*, 1194–1202. https://doi.org/10.1016/j.molp.2020.06.009.

45. Sali, A., and Blundell, T.L. (1993). Comparative protein modelling by satisfaction of spatial restraints. J. Mol. Biol. *234*, 779–815. https://doi.org/10.1006/jmbi.1993.1626.

46. Shen, M.Y., and Sali, A. (2006). Statistical potential for assessment and prediction of protein structures. Protein Sci. *15*, 2507–2524. https://doi.org/10.1110/ps.062416606.

47. Lovell, S.C., Davis, I.W., Arendall, W.B., 3rd, de Bakker, P.I.W., Word, J.M., Prisant, M.G., Richardson, J.S., and Richardson, D.C. (2003). Structure validation by Cα geometry: φ,ψ and Cβ deviation. Proteins *50*, 437–450. https://doi.org/10.1002/prot.10286.

48. Raman, S., Vernon, R., Thompson, J., Tyka, M., Sadreyev, R., Pei, J., Kim, D., Kellogg, E., DiMaio, F., Lange, O., et al. (2009). Structure prediction for CASP8 with all-atom refinement using Rosetta. Proteins *77 Suppl 9*, 89–99. https://doi.org/10.1002/prot.22540.

49. Zhang, Y., and Skolnick, J. (2004). Scoring function for automated assessment of protein structure template quality. Proteins *57*, 702–710. https://doi.org/10.1002/prot.20264.

50. Ovchinnikov, S., Park, H., Varghese, N., Huang, P.S., Pavlopoulos, G.A., Kim, D.E., Kamisetty, H., Kyrpides, N.C., and Baker, D. (2017). Protein structure determination using metagenome sequence data. Science *355*, 294–298. https://doi.org/10.1126/science.aah4043.

51. Lindorff-Larsen, K., Piana, S., Palmo, K., Maragakis, P., Klepeis, J.L., Dror, R.O., and Shaw, D.E. (2010). Improved side-chain torsion potentials for the Amber ff99SB protein force field. Proteins *78*, 1950–1958. https://doi.org/10.1002/prot.22711.

52. Pronk, S., Páll, S., Schulz, R., Larsson, P., Bjelkmar, P., Apostolov, R., Shirts, M.R., Smith, J.C., Kasson, P.M., van der Spoel, D., et al. (2013). Gromacs 4.5: a high-throughput and highly parallel open source molecular simulation toolkit. Bioinformatics *29*, 845–854. https://doi.org/10.1093/bioinformatics/btt055.

53. Paesani, F., Zhang, W., Case, D.A., Cheatham, T.E., 3rd, and Voth, G.A. (2006). An accurate and simple quantum model for liquid water. J. Chem. Phys. *125*, 184507. https://doi.org/10.1063/1.2386157.

54. Cheatham, T.E.I., Miller, J.L., Fox, T., Darden, T.A., and Kollman, P.A. (1995). Molecular dynamics simulations on solvated biomolecular systems: the particle mesh Ewald method leads to stable trajectories of DNA, RNA, and Proteins. J. Am. Chem. Soc. *117*, 4193–4194. https://doi.org/10.1021/ja00119a045.

55. Ryckaert, J.P., Ciccotti, G., and Berendsen, H.J. (1977). Numerical integration of the cartesian equations of motion of a system with constraints: molecular dynamics of n-alkanes. J. Comput. Phys. *23*, 327–341. https://doi.org/10.1016/0021-9991(77)90098-5.

56. Berendsen, H.J.C., Postma, J.P.M., van Gunsteren, W.F., Di Nola, A., and Haak, J.R. (1984). Molecular dynamics with coupling to an external bath. J. Chem. Phys. *81*, 3684–3690. https://doi.org/10.1063/1.448118.

57. Parrinello, M., and Rahman, A. (1981). Polymorphic transitions in single crystals: a new molecular dynamics method. J. Appl. Phys. *52*, 7182–7190. https://doi.org/10.1063/1.328693.

58. Humphrey, W., Dalke, A., and Schulten, K. (1996). VMD: visual molecular dynamics. J. Mol. Graph. *14*, 33–38. https://doi.org/10.1016/0263-7855(96)00018-5.

59. Meagher, K.L., Redman, L.T., and Carlson, H.A. (2003). Development of polyphosphate parameters for use with the AMBER force field. J. Comput. Chem. *24*, 1016–1025. https://doi.org/10.1002/jcc.10262.

60. Allnér, O., Nilsson, L., and Villa, A. (2012). Magnesium ion-water coordination and exchange in biomolecular simulations. J. Chem. Theor. Comput. *8*, 1493–1502. https://doi.org/10.1021/ct3000734.

61. Wang, J., Wolf, R.M., Caldwell, J.W., Kollman, P.A., and Case, D.A. (2004). Development and testing of a general amber force field. J. Comput. Chem. *25*, 1157–1174. https://doi.org/10.1002/jcc.20035.

62. Case, D.A., Ben-Shalom, I.Y., Brozell, S.R., Cerutti, D.S., Cheatham, T.E.C., III, Cruzeiro, V.W.D., Darden, T.A., Duke, R.E., Ghoreishi, D., Gilson, M.K., et al. (2018). *AMBER 2018*. San Francisco (University of California).

63. Sousa da Silva, A.W., and Vranken, W.F. (2012). Acpype - AnteChamber PYthon parser interfacE. BMC Res. Notes *5*, 367. https://doi.org/10.1186/1756-0500-5-367.

64. Kumari, R., Kumar, R.; Open Source Drug Discovery Consortium, and Lynn, A. (2014). g_mmpbsa–a GROMACS tool for high-throughput MM-PBSA calculations. J. Chem. Inf. Model. *54*, 1951–1962. https://doi.org/10.1021/ci500020m.

STAR★METHODS

KEY RESOURCES TABLE

REAGENT or RESOURCE	SOURCE	IDENTIFIER
Antibodies		
Anti His-Tag Mouse Monoclonal Antibody	TransGen Biotech, China	Cat# HT501-01
Anti GST-Tag Rabbit Polyclonal Antibody	CWBIO, China	Cat# CW0084M
Sf-Atg8 polyclonal antibody, Rabbit	laboratory-owned	GenBank: MF069154.1
Sf-Cathepsin L polyclonal antibody, Mouse	laboratory-owned	GenBank: HQ110065.1
CY3 Conjugated AffiniPure Goat Anti-mouse IgG (H+L)	Boster, China	Cat# BA1031
FITC Conjugated AffiniPure Mouse Anti-Rabbit IgG (H+L)	Boster, China	Cat# BA1105
Chemicals, peptides, and recombinant proteins		
GST agarose gel	Yeasen, China	20507ES10
guanosine triphosphate	Mei5Bio	G78452
Harmine, ≥98%	Bidepharm, China	BD14622
X-α-Gal	Yeasen, China	10903ES60
aureobasidin A	Yeasen, China	60231ES
Critical commercial assays		
Matchmaker® Gold Yeast Two-Hybrid System	TAKARA Clontech, China	630489
soluble protein His-tag protein purification kit	CWBIO, China	CW0894S
FuGENE® HD Transfection Reagent	Promega, USA	E2311
T7 RiboMAX™ Express RNAi System	Promega, USA	P1700
E.Z.N.A.® Endo-Free Plasmid Mini Kit II	Omega, USA	D6950-01
Eastep® Super Total RNA Extraction Kit	Promega, USA	LS1040
Fast Site-Directed Mutagenesis Kit	TIANGEN, China	KM101
Deposited data		
Genome Data of all selected species	NCBI	https://www.ncbi.nlm.nih.gov/
Experimental models: Cell lines		
Spodoptera frugiperda Sf9 cells	Insect Toxicology Laboratory, College of Plant Protection, SCAU	N/A
Oligonucleotides		
Primers, see Table S3	This paper	N/A
Recombinant DNA		
Plasmid: pET-28a, pCold I and pGEX-4T-1	laboratory-owned	N/A
Plasmid: PIZT-V5/His	laboratory-owned	N/A
Software and algorithms		
TBtools software	Chen et al.[44]	https://doi.org/10.1016/j.molp.2020.06.009
MEGA X	MEGA, USA	https://www.megasoftware.net/
DNAMAN	Lynnon Biosoft, USA	https://www.lynnon.com/
Discovery Studio 2017	Dassault Systèmes BIOVIA, San Diego, USA	N/A

(*Continued on next page*)

Continued

REAGENT or RESOURCE	SOURCE	IDENTIFIER
AMBER 2018	San Francisco: University of California.	N/A
Image-Pro Plus 6.0 software	Media Cybernetics, USA	https://www.epixinc.com/vision_archive/imagepro.htm
SPSS 22.0	IBM, USA	https://www.ibm.com/cn-zh/spss

RESOURCE AVAILABILITY

Lead contact

Further information and requests for resources and reagents should be directed to and will be fulfilled by the lead contact, Guohua Zhong (guohuazhong@scau.edu.cn).

Materials availability

This study did not generate new unique reagents.

Data and code availability

- All data reported in this paper will be shared by the lead contact upon request.
- This paper does not report original code.
- Any additional information required to reanalyze the data reported in this paper is available from the lead contact upon request.

EXPERIMENTAL MODEL AND STUDY PARTICIPANT DETAILS

Cell lines

The *Spodoptera frugiperda* Sf9 cells were kept at the Insect Toxicology Laboratory, College of Plant Protection, South China Agricultural University (Guangzhou, China) and routinely maintained at 27 °C in culture flasks (Nest, China) with Grace's insect cell culture medium containing 10% fetal bovine serum (Gibco, USA). Cell activity detection, cellular morphology subcellular structure and fluorescence staining observation were performed as described in our previous reports.[22]

METHOD DETAILS

Bioinformatics analysis

Genomes of all the species were obtained from the NCBI database (Table S1). Simple HMM search and Blastn (2.2.30+) were used for sequences searching within TBtools software according to the conserved domain or pfam data.[44] Relevant sequences of Rab7, RILP, VPS39, VPS41, FYCO1, OSBP and PLEKHM1 were auto filtered and manual selected from the genome and NCBI database. The NCBI conserved domain search (https://www.ncbi.nlm.nih.gov/Structure/cdd/wrpsb.cgi) was used for the domain search. MEGA X (MEGA, USA) was used for phylogenetic analysis. Furthermore, DNAMAN (Lynnon Biosoft, USA) was used to analyze the amino acid sequence similarity of Rab7 and RILP.

Point mutations and truncated expression

The primers (Table S3) were designed by Primer Premier 5.0 (Premier, Canada). Total RNA was extracted by an Eastep® Super Total RNA Extraction Kit (Promega, USA), and cDNA was generated by a FastKing RT Kit (TIANGEN, China). The point mutations were processed following the instructions of the Fast Site-Directed Mutagenesis Kit (Tiangen, China). All these gene sequences were cloned and inserted into a cloning vector, pMD19T-simple (Takara, China). The sequences were screened and verified by sequencing (TsingKe, China), then kinds of recombinant plasmids were constructed for various purposes, including pET28a, pCold I and pGEX-4T-1 for expression, pGADT7 and pGBKT7 for yeast two-hybrid system, and PIZT-V5/His for overexpression.

Yeast two-hybrid system

The interactions between Rab7 and RILP were analyzed by yeast two-hybrid assays. All the DNA sequences of Rab7 and RILP were inserted into pGBKT7 or pGADT7 vectors (TAKARA Clontech, China). After co-transfection of pGBKT7 and pGADT7, the yeast colonies were grown in DDO/X, SD/-Leu/-Trp double dropout media (Clontech, China) containing X-α-Gal (40 μg/mL, Yeasen, China) and QDO/X/A, SD/-Ade/-His/-Leu/-Trp quadruple dropout media (Clontech, China) containing X-α-Gal and aureobasidin A (200 ng/mL, Yeasen, China) agar plates. TDO/X/A, SD/-His/-Leu/-Trp triple dropout media containing X-α-Gal and aureobasidin A agar plates were also sometimes used. The biochemical incubator was cultured inverted at 30°C. The results (Figures S19–S24) were judged based on the state and color of the colonies (Positive, blue colonies on QDO/X/A or TDO/X/A plates; Negative, no colonies on DDO/X, QDO/X/A or TDO/X/A, or white colonies on QDO/X/A or TDO/X/A plates).

GST pull-down assay

The prokaryotic expression plasmids pET-28a, pCold I and pGEX-4T-1 were used, and purification of the protein was carried out using a soluble protein His-tag protein purification kit (CWBIO, China) and a GST agarose gel (Yeasen, China). After ultrasonication, the supernatants of GSTs' procaryotic lysates were divided into three centrifuge tubes with GST agarose gel and gently incubated at 4°C for 2 h. After washing with binding buffer, guanosine triphosphate (2 mM GTP, Mei5Bio, China) was mixed with the supernatant of His-tagged proteins' procaryotic lysates and then were divided into three different GST fillers. The proteins were gently mixed and incubated overnight at 4°C. Elution buffer supplemented with reduced glutathione (Bidepharm, China) was used to recover the supernatants. The recovered supernatants were detected with western blotting for the His-tag (Anti His-Tag Mouse Monoclonal Antibody, TransGen Biotech, China) and GST-tag (Anti GST-Tag Rabbit Polyclonal Antibody, CWBIO, China).

Model construction

The X-ray crystal structure (PDB: 1YHN) of the structure basis of RILP recruitment by Rab7 was used as the template for modeling Sf-Rab7, and Discovery Studio 2017 (DS2017, Dassault Systèmes BIOVIA, San Diego, USA) software was employed. In summary, the alignment of Sf-Rab7 and Hs-Rab7 sequences was conducted with the MODELER program,[45] and the homology model was built. In addition, the number of models with a high optimization level was set to 20, and other parameters were set to the default values. Furthermore, the structure with the lowest probability density function (PDF) energy and DOPE score[46] was selected as the candidate model and then further assessed by Verify Protein (Profiles-3D) and Ramanchandran Plot protocols.[47] The N-terminal Sf-RILP (Sf-RILP-N, 31-169aa) was constructed by the Robetta server (http://new.robetta.org/) using the *ab initio modeling* method,[48] which provides a predicted confidence value that corresponds to the average pairwise TM-score of the top 10 Rosetta scoring models.[49,50]

Dynamic optimization of Sf-RILP-N

The molecular dynamics simulation (MDs) was applied to optimize the Sf-RILP-N model. The AMBER99SB-ILDN force field[51] implemented in the GROMACS MD package[52] version 2016.4 was used as the parameter for protein and ions. The protein was immersed in a rhombic dodecahedron box, further solvated with TIP3P water molecules, and then neutralized by adding Na^+ and Cl^- ions at a concentration of 0.15 via the genion tool of the GROMACS package. The simulation was then carried out using Gromacs. Electrostatic interactions have been taken into account by means of the particle mesh Ewald (PME) method,[53] and the bond lengths and angles have been constrained using the LINCS algorithm.[54] The system was first minimized by 5000 steps of the steepest descent algorithm with an emstep of 0.1 nm and an emtol of 1000 $kJ*mol^{-1}* nm^{-1}$, followed by 5000 steps of the conjugate gradient at an emstep of 0.01 nm and an emtol of 100 $kJ*mol^{-1}* nm^{-1}$. The system was then equilibrated for 200 ps with a time step of 1.0 fs at a constant temperature of 310.15 K using the velocity-rescale method[55] with a coupling constant of 0.2 ps during sampling, while the pressure was kept constant at 1 bar using Berendsen's method[56] with a coupling constant of 0.5 ps. The subsequent 500 ns production was carried out with a time step of 2.0 fs at the same temperature coupling, while pressure was measured using the Parrinello-Rahman barostat[57] with a coupling constant of 2.0 ps during sampling. All standard analyses were calculated using the tools of the GROMACS package. Images were produced with VMD,[58] pymo (education version 1.7, The PyMOL

Molecular Graphics System, Schrödinger LLC.), and DS 2017, and graphs were obtained with the Grace program (http://plasma-gate.weizmann.ac.il/Grace/).

Docking simulation of Sf-Rab7 and Sf-NRILP

The most stable residues, Sf-NRILP (31-91aa), at 500 ns were selected for docking with sf-Rab7 by using the DOCK PROTEINS (ZDOCK) protocol in DS2017. The docking parameter of "Angular step size" was set to 15, "Distance Cutoff" was 10, the maximum number of clusters was 100, and other parameters were set *to* default values. All poses with ZDOCK scores greater than 12 were further optimized by the Refine Docked Proteins (RDOCK) protocol with the default parameters.

Dynamic monitoring of the recruiting process

The AMBER99SB-ILDN force field was used as the parameter for proteins and ions but not Mg^{2+}. Meanwhile, the PREP file, FRCMOD parameters of GTP (Contributed by Carlson H. A.[59]) and Mg^{2+} (contributed by Jesper Sorensen[60]) were downloaded from the AMBER parameter database (http://research.bmh.manchester.ac.uk/bryce/amber/). Then, the general AMBER force field (GAFF)[61] and AMBER99SB-ILDN force field were used as the parameters for GTP and Mg^{2+} to obtain the GROMACS topologies file by using the tleap and parmchk2 program in AmberTools18[62] and the Acpype program.[63] All of the molecular dynamics simulation methods are consistent with those described above, except that the time of production is 100 ns. Meanwhile, Sf-NRILP mutants (L57A, E58A, L59A, L60A and E61A) were constructed by DS2017 and used the same simulation methods mentioned above for monitoring the changes.

Binding energy calculation

The molecular mechanics Poisson-Boltzmann surface area (MM-PBSA) analysis was performed through GROMACS for the analysis of the energy changes by using a g_mmpbsa tool[64] in the last 20 ns equilibrium trajectory with a total of 200 frames. The nonpolar solvation energy (using the solvent accessible surface area (SASA) model in this study), molecular mechanics potential energy, and polar solvation energy were calculated with default parameters for Sf-RAB7, Sf-NRILP and the complex, respectively. The binding energy was then calculated by MmPbSaStat.py (http://rashmikumari.github.io/g_mmpbsa) and decomposed on a per residue basis as the energy contribution.

Overexpression of Rab7 and RILP

Plasmids containing overexpressed sequences were digested by restriction endonucleases (Thermo Fisher, USA) and connected to the insect expression plasmid PIZT-V5/His with T4 ligase (TAKARA, China). The plasmid was extracted with an E.Z.N.A.® Endo-Free Plasmid Mini Kit II (Omega, USA), and FuGENE® HD Transfection Reagent (Promega, USA) was used to transfect the cells. After 24 h, Sf9 cells were treated with 0.05 mM harmine (98%, Bidepharm, China), and cell immunofluorescence was carried out. The primary antibody was Sf-Atg8 polyclonal antibody (1:1000, MF069154.1, GeneCreate, Wuhan, China) and Sf-Cathepsin L polyclonal antibody (1:1000, HQ110065.1, laboratory-owned), and the secondary antibody was CY3 Conjugated AffiniPure Goat Anti-mouse IgG (H+L) and CY3 Conjugated AffiniPure Goat Anti-rabbit IgG (H+L) (Boster, China). The images were taken by a laser confocal microscope (Nikon A1, Japan) and the fluorescence analysis were carried out with the built-in Nikon software.

RNA interference of Rab7 and RILP

The RNAi procedure was performed with reference to the longer double-stranded RNA (dsRNA) synthesis step in the T7 RiboMAX^{TM} Express RNAi System (Promega, USA). The obtained dsRNA was transfected into Sf9 cells after overnight culture and then treated with 0.05 mM harmine for 24 h. cell immunofluorescence was carried out and the primary antibody, Sf-Atg8 polyclonal antibody and Sf-Cathepsin L polyclonal antibody, were used. The secondary antibody was CY3 Conjugated AffiniPure Goat Anti-mouse IgG (H+L) and FITC Conjugated AffiniPure Mouse Anti-Rabbit IgG (H+L) (Boster, China). The images were taken by an inverted fluorescence microscope (Nikon 600 L, Japan) and merged with the built-in Nikon software. Fluorescence statistics were performed using Image-Pro Plus 6.0 software (Media Cybernetics, USA) and area, diameter (mean), density (mean), and IOD were evaluated. The Cathepsin L-positive points of red fluorescence were selected with intensity ≥ 15, and the Atg8-positive points of green fluorescence were selected with intensity ≥ 20.

QUANTIFICATION AND STATISTICAL ANALYSIS

At least five fluorescence pictures were taken under fixed parameter of each treatment and more than twice biological replications were carried out during the overexpression and RNAi experiments. Original fluorescence data were generated from the built-in Nikon software of inverted fluorescence microscope or laser confocal microscope, and from the Image-Pro Plus 6.0 software. The data were analyzed with SPSS 22.0 (IBM, USA) with *t-test* and one-way ANOVA analysis.